THE JOURNAL OF PHYSICAL CHEMISTRY C
A JOURNAL OF THE AMERICAN CHEMICAL SOCIETY

pubs.acs.org/JPCC

Article

Combustion Reaction Dynamics of Nano-Aluminum and Polyvinylidene Fluoride Composites. Part II: Multiscale Computational Simulations

Daniel Olsen, Erik Hagen, Michael R. Zachariah, and Min Zhou*

Cite This: *J. Phys. Chem. C* 2026, 130, 8972–8986

Read Online

ACCESS | Metrics & More | Article Recommendations | Supporting Information

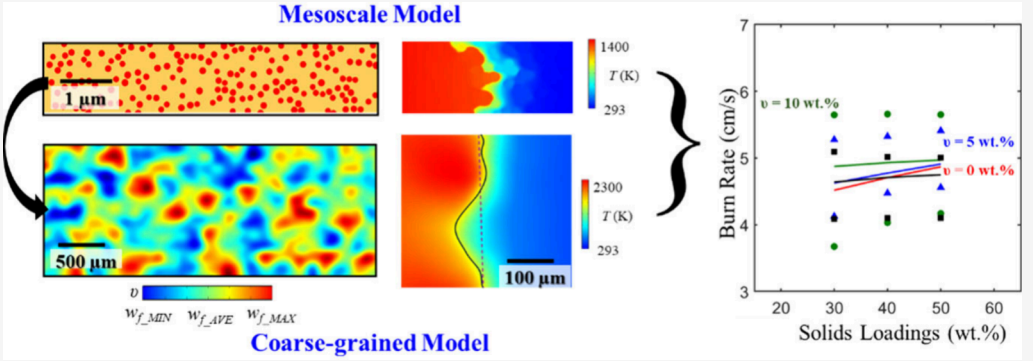

ABSTRACT: In Part I (*J. Phys. Chem. C* **2026**, 10.1021/acs.jpcc.6c00579) of this two-part series, experiments were conducted to characterize the reaction propagation in aluminum and polyvinylidene fluoride (Al/PVDF) composites. Here, we report the development of integrated models at two size scales to gain insights into the experimental observations. The two models have different but mutually reinforcing spatial resolutions: the mesoscale model provides explicit resolution of the particle−polymer heterogeneous microstructure and focuses on the material response at the particle level (∼5 μm), and the coarse-grained model phenomenologically captures the effects of particle agglomeration and density fluctuations at higher length scales (∼1500 μm). The coarse-grained model is informed by and calibrated using results from the lower-scale model in terms of reaction kinetics. The mesoscale model is used to show how particle size, interparticle distance, and solids loading influence the burn rate. It is found that heat flux, temperature distribution, and burn rate at the interparticle level are strongly affected by particle size and interparticle distance. On the other hand, the coarse-grained model allows large-scale temperature distribution fluctuations and flame front corrugation observed in experiments to be quantitatively assessed. The results agree with the experimental observations in terms of statistical variations in the temperature field, local burn rate, and burn front morphology. Overall, heterogeneities at both the micro interparticle scale and in the form of higher-scale particle clustering are found to significantly affect the material response and act to obscure the dependence of burn rate on solids loading.

1. INTRODUCTION

Energetic materials (EM) display a range of reaction behaviors which can be controlled by combinations of materials, microstructures, and manufacturing processes. The addition of nanoparticles to a composite is one increasingly popular method of altering reaction ignition and propagation in an EM.[1,2] Specifically, aluminum nanoparticles have been a major focus in this area. Aluminum has long been used as an additive fuel for energetic materials due to its higher energy density and reactivity.[3] Combinations of aluminum particles with different energetic crystals and polymers are often created for tailorable properties.[4] One reaction of note is the fluorination of aluminum in fluorine-containing polymers.[5] The reaction of aluminum and fluorine has a higher energy density per mole than the aluminum−oxygen reaction. Fluorine-containing polymers, such as polyvinylidene fluoride (PVDF), can be used as binders in many energetic composites, which has led to the increased interest and study of Al/PVDF combinations and their properties.[6]

Burn rate is a common metric used to quantify the energy release rate and the stability of an energetic material. Even though the fluorination reaction in Al/PVDF composites has a high energy density as noted above, Al/PVDF composites have

Received: January 27, 2026
Revised: April 27, 2026
Accepted: May 12, 2026
Published: June 19, 2026

ACS Publications

© 2026 American Chemical Society

Downloaded from pubs.acs.org/jpccck/article-pdf/130/26/8972/6516086/acs.jpcc.6c00580.pdf by UNIV OF CALIFORNIA RIVERSIDE user on 29 August 2026

relatively low burn rates compared to other materials.[7] Improving and controlling the burn rate through applied external energy[8] or microstructure[9] can lead to new use cases and tailored performance. This is the second part of a two-part study that focuses on this issue. Part I reports the results of experiments on ink-printed composites of Al/PVDF with novel diagnostics including high-speed microscopy and high-speed pyrometry.[10] These diagnostic methods provide a greater level of detail of the thermal field and therefore aspects such as flame depth. The experiments show that Al/PVDF samples with solids loadings between 30 and 50 wt % have similar average burn rates. This observation is in contrast to the previously established understanding that increasing the amount of thermally conducting particles in a system increases the burn rate.[11,12] This raises the question of what causes the ostensible discrepancy in this case. Previous studies have shown that particle agglomeration[13] and particle size[14] can have significant effects on reaction initiation and burn rate. For example, Pivkina et al.[14] found that nanosized aluminum particles and finer energetic crystals significantly increased the burn rate of energetic composites. This trend is contrary to another general observation that burn rate decreases with decreasing particle size.[15] Fukuchi[16] found that particle clusters reduced the burn rate as well. Aluminum particles are known to have a passivated layer of aluminum oxide that can affect reaction times depending on its thickness.[15] One goal of this paper (Part II) is to explore how the underlying material microstructure heterogeneities can help explain the observations in Part I and to what extent they do so.

Experiments provide physical trends and initial insights into the material response but often do not provide detailed mechanistic understanding. Computational modeling can greatly augment experimental results by providing microscopic explanations of observed physical processes. However, models at different scales have different spatial resolutions and therefore capture different physical phenomena, each with inherent limitations.

At the finest scale, molecular dynamics (MD) simulations resolve atomic-level interactions but are limited to short time scales and small domains. For example, Gao et al.[17] used MD simulations to study the effects of aluminum particle shape and oxide layer thickness on Al/PVDF reaction kinetics at the ångstrom scale. While such models provide valuable insights into local reaction mechanisms, they are too small to capture reaction propagation effects.

At the mesoscale, models can explicitly resolve individual particles across the size range between nanometers and hundreds of micrometers. These models are associated with significant computational cost due to the wide range of coupled physical and chemical processes involved. Models such as those of Gallier et al.[18] and Washburn et al.[19] study the burning time of a single fixed aluminum particle using 2D Lagrangian frameworks and simplified chemical reaction descriptions. The displacement of particles is also an important consideration, as demonstrated by Wang et al.[20] and Bojko et al.[21] using multiparticle models. Because they use constant reaction rates, these models lack the ability to capture the interplay between species diffusion and reaction kinetics at the particle/interparticle scale.

At the macroscale, homogenized models can resolve reaction propagation over longer distances and capture the structure of reaction zones at scales up to tens of millimeters or even meters. These models lack sufficient resolution for small-scale heterogeneities and mechanisms at the particle and interparticle scale.[22] Such models include those of Najim et al.[23] and Chakraborty et al.[24] and involve significant simplifications. For example, the model of Chakraborty et al. uses a spatially nonuniform reaction kinetics description in an otherwise homogeneous setting to phenomenologically capture nonuniform reaction fronts. The model does not resolve species concentration, interdiffusion between the reactants, or other mechanisms that drive the fluorination reaction.

To integrate the advantages of both scales, we develop a multiscale model framework by integrating two models that focus on different size scales in a mutually informative manner. Specifically, the mesoscale model tracks reaction initiation and propagation at the particle level and captures interparticle interactions. Because intermixing of the species is a precondition for reaction, this model resolves the interdiffusion between the particles and the polymer, thereby allowing the competing effects of reaction kinetics and diffusion in the microstructure setting to be analyzed. This model is ideally suited for studying the effects of particle size, distribution, and particle density, which is related to the solids loading of the material. The choice of these mesoscale parameters depends on the overall material solids loading and larger-scale heterogeneities (or particle clustering) captured by a higher-scale coarse-grained model that focuses on the reaction propagation processes over the scale of hundreds of microns and the effects of regional fluctuations in particle density at the macroscopic scale. While the formulation of the microstructure space for the mesoscale model is guided by the macroscopic material attributes and the coarse-grained model, the higher-scale model is informed by the mesoscale model in terms of the homogenized reaction kinetics and material properties it needs for input.

The focus of this paper is on gaining insights into the experimental observations in Part I.[10] The fine-grained mesoscale model focuses on the explicit resolution of the particle−polymer distribution and its effects on the reaction initiation. The coarse-grained model uses the results of the mesoscale model as input and phenomenologically accounts for the effects of larger-scale spatial fluctuations in the particle distributions at the macroscopic size scale of the experiments. Comparisons are made between simulations and experiments. The particular quantities of interest are peak temperature, flame length, burn rate, and heat flux. The calibrated models are used to explore and explain a perplexing trend seen in the results of the experiments. Specifically, it is found that large-scale fluctuations in particle density or particle clustering cause the burn front corrugation observed in the experiments. Furthermore, the severely corrugated burn front gives rise to large variations in local burn rate. As a result, the wide distributions of the local burn rate obscure the relationship between the average burn rate and overall average solids loading of the material, thereby providing an explanation for the ostensibly different trends in Part I and previous reports.[10,11]

2. MODEL APPROACH

Material heterogeneities are the primary drivers of the complexities in the material behavior observed in experiments. As such, the models are designed to capture material heterogeneities at the relevant scales, from the particle/interparticle scale (~5 μm) to the macroscale of the burn front thickness, reaction propagation distance, and large-scale

Downloaded from pubs.acs.org/jpccck/article-pdf/130/26/8972/6516086/acs.jpcc.6c00580.pdf by UNIV OF CALIFORNIA RIVERSIDE user on 29 August 2026

https://doi.org/10.1021/acs.jpcc.6c00580
J. Phys. Chem. C 2026, 130, 8972−8986

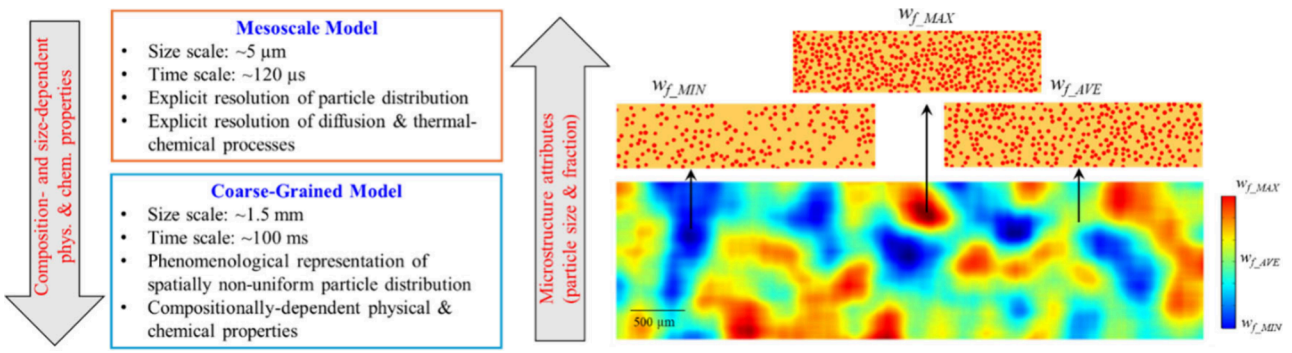

Figure 1. Integrated mesoscale microstructure-explicit model and coarse-grained macroscale model. The mesoscale model informs and provides parameters for the coarse-grained model and the coarse-grained model guides the determination of microstructure attributes of the mesoscale model. The governing equations for these models are discussed in Section 2.2.

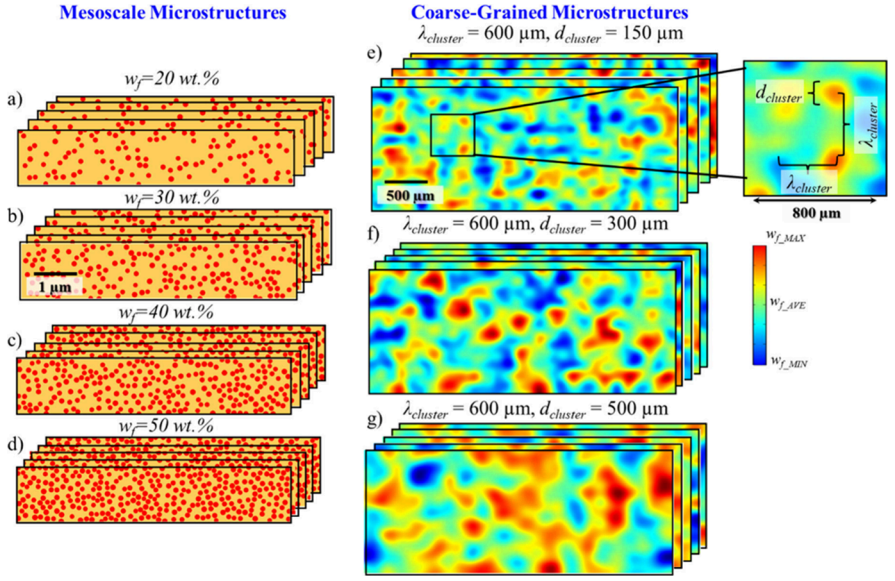

Figure 2. Statistically equivalent microstructure sample sets (SEMSS) generated and used, (a−d) for the mesoscale model and (e−g) for the coarse-grained model. Each case has five randomly instantiated samples for statistical characterization for material behavior.

particle distribution fluctuations (~1.5 mm). These two scales are illustrated in Figure 1. Section 2.1 focuses on the range of material settings considered and the statistical descriptions for the two models. Section 2.2 describes the governing equations and material and reaction models for both the coarse-grained and mesoscale models. The differences and the relationships between the mesoscale model and the coarse-grained model are outlined. Figure 1 also shows the key features of the two levels of models, the physics they capture, and how they inform each other.

2.1. Materials and Material Models

The mesoscale model explicitly resolves the nano-aluminum particle and PVDF matrix morphology and distribution. The three particle diameter ranges considered are 50−70 nm, 90−110 nm, and 190−210 nm, which track the attributes of the materials used in the experiments in Part I, as seen in the SEM images. The particles have a core−shell structure with the active aluminum core comprising 90% by weight and the passivated shell making up the rest. The particle diameters conform to Gaussian distributions with prescribed averages and standard deviations. A distribution with an average size of 100 nm and a standard deviation of 5 nm is shown in Figure S1 of the Supporting Information. The three cases considered have the average-standard deviation combinations of (60, 5), (100, 5), and (200, 5). During the microstructure generation process, the particles are assigned random locations until the required solids loading level is reached. The algorithm does not allow particle overlap or interpenetration. Four solids loading levels between 20 and 50 wt % are considered, as shown in Figure 2a−d. In each case, a statistically equivalent microstructure sample set (SEMSS) with five randomly instantiated samples are generated and used. The total number of samples studied is 4 × 5 = 20. Further characterization of the differences among these mesoscale microstructure sample sets through a nearest neighbor distance (NND) analysis is presented at the end of this section.

The preparation process for the nAl/PVDF polymer composites has been shown by Messer et al.[25] to lead to particle clustering with cluster size scales around 10−30 μm and cluster-to-cluster solids loading density fluctuations between 5 and 20 wt %. The coarse-grained model, following the process shown in Figure 1, resolves such regional variations in particle density in a phenomenological manner rather than the explicit morphology of individual particles as the mesoscale model does. The heterogeneities at the mesoscale and the macroscale are not totally independent of each other.[26]

Downloaded from pubs.acs.org/jpccck/article-pdf/130/26/8972/6516108/acs.jpcc.6c00580.pdf by UNIV OF CALIFORNIA RIVERSIDE user on 29 August 2026

https://doi.org/10.1021/acs.jpcc.6c00580
J. Phys. Chem. C 2026, 130, 8972−8986

Specifically, particle size variations in nano to micron size scales can influence the distributions of particles and particle clustering, with the clusters being up to 10s of microns in size.[27] Three cases are analyzed, as shown in Figure 2. Each case involves five randomly instantiated samples, just like in the mesoscale cases. In the three cases considered, the average diameter of the clusters, $d_{cluster}$, are 150 μm, 300 μm, and 500 μm, respectively, as shown in Figure 2. The cutoff of $d_{cluster}$ is when the surrounding solids loading changes by more than 5% of the maximum/minimum solids loading value. The overall model size is 1800 × 3000 μm, sufficiently large to capture several periods of clusters, resolve the structure of corrugated burn fronts, and track sufficient length of burn front propagation. The coarse-grained model instantiations with particle density fluctuations are generated through Gaussian random fields. Two parameters control the attributes of the samples, the spatial wavelength or distance between cluster peaks (or troughs), $\lambda_{cluster}$, and the size of the clusters, $d_{cluster}$. The particle density at each location determines the material property and reaction kinetics parameters at that location. For each of the three cluster sizes ($d_{cluster}$ = 150 μm, 300 μm, and 500 μm), three levels of average solids loading w_{f_AVE} are considered. For each of the three w_{f_AVE} levels, three levels of solids loading variation ($v_{var.}$) are considered: ± 0 wt % (homogeneous), ± 5 wt %, and ± 10 wt %. In total, 57 coarse-grained microstructure cases are considered. The naming convention for the coarse-grained samples is w_{f_AVE} ± $v_{var.}$, $\lambda_{cluster}$, $d_{cluster}$. These cases are listed in Table S1 in the Supporting Information, along with their case IDs. Since five random instantiations are generated and used for each case, the total number of samples studied is 57 × 5 = 285.

To obtain quantitative measures for the particle distributions in the mesoscale models, the nearest neighbor distance (NND) distributions for the mesoscale microstructures in Figure 2a−d are calculated. The NND distribution is a statistical measure for the density distribution of the distance between the centers of each particle and its nearest neighbor for all particles in a sample. The resulting distributions for the average particle size of d_{ave} = 100 nm (which is the average size in Part I) are shown in Figure S3. The averages for each particle size are shown in Table 1. Overall, at the same solids loading level, the average

Table 1. Average NND for Each Particle Size and Solids Loading Considered in the Study

	20 wt %	30 wt %	40 wt %	50 wt %
60 nm	84.3 nm	65.3 nm	60.0 nm	55.5 nm
100 nm	142.2 nm	123 nm	114 nm	107 nm
200 nm	286.6 nm	259.4 nm	237.5 nm	213.8 nm

NND is larger for larger particle sizes. Furthermore, the averages between solids loadings in the 60 and 100 nm cases vary by less than 16% of the particle size. This results in similar distances between particles in all cases. These correlations will be used to explain the trends in reaction behavior later in Section 3.2.

2.2. Governing Equations

Capturing the reaction behavior of aluminum composites can be a challenge.[28] This section outlines the underlying physics and the necessary equations to model the material behavior. The generally understood reaction involving aluminum is as follows. As heat is deposited through mechanical loading or other mechanisms, the material surrounding the metallic particles (e.g., PVDF) undergoes a phase change, such as melting or sublimation. Decomposition is likely, as the thermal decomposition point of PVDF is 600−700 K. Volume expansion causes bulk flow that pushes the metal particles along.[19] As temperature increases, the particles reach a molten state as well, albeit at a higher temperature than the polymer, due to their higher melting temperature of ∼930 K, eventually transforming into liquid droplets. The resulting multiphase flow consists of both the molten phases and gaseous products of the reacting material.[29] The complexity of the processes is 2-fold. First, the reaction does not take place directly at the reaction front. Second, the molten particles can "agglomerate".[30] Since a portion of the reaction takes place further away from the reaction front, heat generation from the reaction is not necessarily at the reaction surface. Figure 3 illustrates the

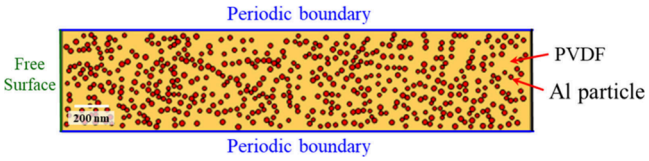

Figure 3. An illustration of the configuration of the mesoscale microstructure-explicit model along with the boundary conditions.

configuration of the mesoscale model that aims to resolve the relevant processes through explicit account of particle-binder distribution and relevant thermal, mechanical, chemical, and transport processes. The boundary conditions are such that outflow through the left-hand free surface is allowed, the top and bottom surfaces are periodic, and the right-hand surface is fixed. The right-hand surface treatment is not consequential because all simulations stop before reactions from the left reach the right end. Both models are 2D for computational efficiency. Although 3D simulations may capture a broader range of effects, 2D simulations have been shown to adequately capture average burn rates and corrugation trends.[21,24] Specifically, the average burn rate between 2D and 3D calculations is similar in general. The scatter in burn rate due to heterogeneities is broader in 3D. The difference between 2D and 3D is larger when the burn rate is higher. Because the burn rate in this study is relatively low, the average burn rate would be quite similar if a 3D model is used.

The reaction between aluminum particles and their surroundings involves complex chemical pathways with multiple reaction steps.[19,31] These networks can require tracking dozens of species and reactions to fully resolve, which will become computationally complex when hundreds of particles are simulated. To capture the key steps, a simplified skeletal scheme from the preignition reaction to the fluorination of aluminum is summarized below.[32] This reaction scheme is under anaerobic conditions,[33−35] due to the dominance of fluorination as an exothermic reaction.

$$\begin{cases} (\mathrm{A})\ Al_2O_3 + -(C_2H_2F_2)_n - \rightarrow (C_xH_yF_z) + HF_{(g)} \\ (\mathrm{B}) -(C_2H_2F_2)_n - \rightarrow (C_xH_yF_z) + HF_{(g)} + C \\ (\mathrm{C})\ (C_xH_yF_z) \rightarrow HF_{(g)} + C \\ (\mathrm{D})\ 2Ai + 6HF_{(g)} \rightarrow 2AlF_3 + 3H_{2(g)} \end{cases} \quad (1)$$

The initial stage (A) in eq 1 starts with a preignition reaction that initiates around 723 K and is known to be catalyzed by the

Downloaded from pubs.acs.org/jpccck/article-pdf/130/26/8972/6516108/acs.jpcc.6c00580.pdf by UNIV OF CALIFORNIA RIVERSIDE user on 29 August 2026

https://doi.org/10.1021/acs.jpcc.6c00580
J. Phys. Chem. C 2026, 130, 8972−8986

presence of the aluminum oxide shell. The subsequent reactions (B) and (C) are further decompositions of PVDF into HF and other species. We consider the first three reactions as endothermic and HF-producing. These will not be considered through a specific Arrhenius relation but as phase changes through property parameter changes to reduce the complexity of tracking chemical kinetics.[36,37] The dominant chemical reaction and the heat release step is the fluorination of aluminum (D). As the surrounding polymer begins to decompose, HF is produced and diffuses into the aluminum particle, resulting in reaction between the species. Incomplete reactions and HF loss to the gas phase are possible but are not explicitly modeled. The net effect of these losses is implicitly captured through the reaction kinetics parameters, which are calibrated using experimental and MD simulation data. These reactions are simplified into a single reaction to focus on the fluorination of aluminum, i.e.,

$$\mathrm{Al} + 3\mathrm{PVDF} \rightarrow \mathrm{Prod} \tag{2}$$

Here, the products, which include incomplete products in soot,[38] have been simplified into a single lumped species to decrease the computational cost required to track multiple species, although this constraint can be removed in future works. The reaction kinetics are assumed to follow the Arrhenius relation of

$$k = Ae^{(-E/R_g T)} \tag{3}$$

which gives the reaction rate as

$$r = k \prod_{n \in \mathrm{react}} (c_n)^{-\nu_n} \tag{4}$$

In the above relations, A is the frequency factor, E is the activation energy, R_g is the universal gas constant, ν_n is the stoichiometric coefficient of the nth reactant species, and c_n is the molar concentration of the nth reactant species. In this case, $n = 1$ for Al and $n = 2$ for PVDF. The expression for r accounts for stoichiometry based on the fourth-order reaction presented in eq 1(D) and eq 2[39−41] and is species-dependent. Therefore, the magnitude of r depends on the local species concentration of the reactants. Aluminum fluorination is exothermic, with large amounts of heat release.[5,6,42] The rate of heat release is[22]

$$q_c(\mathbf{x}, t) = r\Delta H \tag{5}$$

where q_c is the heat release per unit volume per unit time and ΔH is the enthalpy of reaction. This source of heat energy intensifies and becomes dominant as the reaction progresses. The initial temperature rise before ignition is based on an externally applied input energy from the left-hand side of the model in Figures 2 and 3.

Reaction kinetics plays a critical role in ignition and burning. Due to the complexity of the reaction noted above, significant simplification is required. Further difficulty comes from the ranges of kinetics relation parameters used to describe the reactions. These ranges are taken from both experimental results and molecular dynamics simulations[11,17,43,44] and are shown in Table 2.

The form of the chemical kinetics relation outlined above can be used at both the mesoscale and the coarse-grained scale. The difference is in the values of A and E used. The parameters from Table 2 are specific to the mesoscale model. The results calculated in Section 3.1 from the mesoscale model are used to determine the kinetics parameters for the coarse-grained

Table 2. Arrhenius Relation Parameters for the Mesoscale Model[11,17,43,44]

	frequency factor (A) ($m^9/(mol^3 \cdot s)$)	activation energy (E)(kJ/mol)	enthalpy of reaction (ΔH)(kJ/mol)
range in literature	9.77×10^5 to 3.189×10^{14}	71−202	5.99−31.05
model	3.2×10^{12}	71	12

model. The higher-scale parameters are necessary to account for the time delay of reaction initiation due to diffusion and intermixing between the particle and binder which are not explicitly resolved otherwise by the coarse-grained model. The effects of species concentration are captured through eq 4. The governing equations for both models share the same form, as the conservation laws remain consistent across both models. The material properties, such as density and thermal conductivity, are also constant across both models. The key difference between the two lies in the context in which they are used (explicit resolution of the particle distribution versus phenomenological account of particle density variation). These models are implemented in COMSOL Multiphysics, using a backward differentiation formula (BDF) to solve the governing equations.

The energy equation accounts for conduction, convection, and heat release from the reaction and is expressed as

$$\rho C_p \frac{\partial T}{\partial t} - \kappa \nabla^2 T + \rho C_p \mathbf{u} \nabla T = q_c \tag{6}$$

here, ρ is mass density, C_p is specific heat under constant pressure, T is temperature, κ is thermal conductivity, $\mathbf{u}$ is velocity, and q_c is the heat released from the exothermic reaction per unit volume per unit time. The remaining system of equations and assumptions is as follows. All materials within the system will start in a condensed "solid" state.[20] Endothermic phase change, such as aluminum melting, is controlled by the material's latent heat and considered along with the specific heat as solved by COMSOL.[45] Mechanical effects, such as stress and displacement due to thermal expansion, are ignored due to the computational difficulty of including mechanical stresses and phase change along with the developing flow of gases. Continuum equations are used to account for the conservation of momentum, mass, and species, as outlined below. The conservation of species is

$$\frac{\partial}{\partial t}(\rho\omega_i) + \nabla \cdot (\rho\omega_i \mathbf{u}) = -\nabla \cdot \mathbf{j}_i + \Lambda_i \tag{7}$$

Where, ω_i is the mass fraction for the i^{th} species, which is the ratio of the i^{th} species mass density to the total mass density. The relationship between c_i (eq 4) and ω_i is

$$\omega_i = \frac{c_i M_i}{\rho} \tag{8}$$

Here, C_i is the concentration of the ith species (reactant or product), M_i represents the molar mass of the ith species, $\mathbf{j}_i$ is the net mass flux of the i^{th} species, and Λ_i is the mass consumption rate of the ith species. The mass consumption rate is

$$\Lambda_i = \nu_i M_i \prod_{i \in \mathrm{react.}} \left(\frac{\rho\omega_i}{M_i}\right)^{-\nu_i} \tag{9}$$

The net mass flux $\mathbf{j}_i$ is written for a multispecies context, which is necessary for the models at both scales.[46] The form is

https://doi.org/10.1021/acs.jpcc.6c00580
J. Phys. Chem. C 2026, 130, 8972−8986

Downloaded from pubs.acs.org/jpcccck/article-pdf/130/26/8972/6516086/acs.jpcc.6c00580.pdf by UNIV OF CALIFORNIA RIVERSIDE user on 29 August 2026

$$\mathbf{j}_i = -\left[\rho D_i^m \nabla(\omega_i) - \rho\omega_i \sum_k D_k^m \nabla(\omega_k)\right] \tag{10}$$

In the above relation, D_i^m is the diffusivity of the ith species, defined as

$$D_i^m = \left(\sum_{k\neq i} \frac{x_k}{D_{ik}} + \frac{x_i}{1-\omega_i}\sum_{k\neq i}\frac{\omega_k}{D_{ik}}\right)^{-1} \tag{11}$$

Here, D_{ik} is the multicomponent Maxwell-Stefan diffusivities in matrix form and x_i is the mole fraction of the i^{th} species which is related to the mass fraction ω_i by

$$\omega_i = x_i\frac{M_i}{\bar{M}} \tag{12}$$

Here, $\bar{M}$ is the average molar mass of the mixture and M_i is the local molar mass of the ith species. The model recognizes the fact that diffusion is activated in earnest when temperature is sufficiently high to cause phase changes (e.g., melting) in the polymer or particles. This is achieved by specifying the temperature dependence of the diffusivities in a manner that is consistent with the rapid enhancement of diffusion associated with phase transformations.

The Navier−Stokes equation specifies the balance of momentum and is written as

$$\rho\frac{D\mathbf{u}}{Dt} = -\nabla p + \nabla\cdot\left[\mu(\nabla\mathbf{u} + (\nabla\mathbf{u})^T) - \frac{2}{3}\mu(\nabla\cdot\mathbf{u})\mathbf{I}\right] \tag{13}$$

Here, μ is the viscosity, and $\mathbf{I}$ is the identity tensor. This model is appropriate and frequently used for subsonic flow. The viscosity of each constituent is specified using a relationship between the Prandtl (Pr) number, the thermal conductivity k_i and the specific heat $C_{P,i}$ of the local material[20] in the form of

$$\mu = \frac{\mathrm{Pr}\kappa_i}{C_{P,i}} \tag{14}$$

The ideal gas equation of state is used to evaluate the density of the product species, i.e.,

$$p_0 = \frac{\rho_i RT}{M_i} \tag{15}$$

where p_0 is the thermodynamic pressure (assumed to be 1 atm), ρ_i is the density of the product species, and R is the universal gas constant. The total pressure consists of the thermodynamic part (eq 15) and a hydrodynamic part which is related to velocity and fluid flow and solved through the compressible Navier−Stokes assumption.[46]

Since the materials are in a solid state initially and are considered as gases during later stages, it is necessary to differentiate whether the local material at any given point is solid or gas. A state variable is used to track the transition between the solid and gas states. The primary effect is a change in the diffusivity of the species based on a linear increase from a lower value around 10^{-12} m^2/s, typical for a condensed phase, and a potential range of values from 10^{-10} m^2/s to 10^{-7} m^2/s for the liquid and gas phases.[47] This increase initiates at 720 K for PVDF and 930 K for aluminum, as shown in Figure S1d. The diffusivities of the products are temperature independent. When a mixture is present, or in the case of the coarse-grained model, the diffusivity is calculated based on eq 16.

Both the mesoscale model and the coarse-grained model use material properties that are dependent on the local concentration of the species. The material properties are continuously updated via the relation

$$a_{\mathrm{Tot}} = \upsilon_{\mathrm{Al}}a_{\mathrm{Al}}(T) + \upsilon_{\mathrm{PVDF}}a_{\mathrm{PVDF}}(T) + \upsilon_{\mathrm{Prod}}a_{\mathrm{Prod}}(T) \tag{16}$$

where, υ_i is the volume fraction of the ith species and a_i is a material property of the ith species. This relation represents a simple rule of mixtures which reasonably approximates the local material properties.[48] The solids loading maps in Figure 2 for both scales are used. Both aluminum and PVDF are assigned temperature-dependent material properties, whereas the alumina layer is assumed to be temperature insensitive. Thermal conductivity, density, and related properties are treated as functions of temperature before the mixture properties are calculated. Their variations as functions of temperature are provided in the Supporting Information (Figure S1) and their ranges are summarized in Table 3.[49−53] While the law of mixtures is not applied to certain parameters such as viscosity and diffusivity as they are species-specific, they can still be influenced by temperature (e.g., the viscosity calculation in eq 14).

Table 3. Ranges of Material Properties for Aluminum and PVDF[49−53]

material	thermal conductivity (W/m·K)	density (kg/m^3)	specific heat (J/kg·K)	species diffusivity (m^2/s)
Aluminum	237−90	2941−1470	900	10^{-10}−10^{-7}
Alumina	36	3970	765	10^{-10}−10^{-7}
PVDF	0.18−0.03	1780−594	1400	10^{-10}−10^{-5}

The initial values of the thermal conductivity, mass density, and specific heat for the constituents are used to calculate the thermal diffusivities of the Al/PVDF composites with different solids loading levels. The results are found to be in general agreement with the diffusivity values measured in Part I as shown in Table 4.

Table 4. Ranges of Experimental vs Computed Thermal Diffusivity Values

thermal diffusivity	30 wt %	40 wt %	50 wt %
Experimental	6.5×10^{-5} m^2/s	7.2×10^{-5} m^2/s	7.7×10^{-5} m^2/s
Computational	2.12×10^{-5} m^2/s	3.06×10^{-5} m^2/s	3.86×10^{-5} m^2/s

3. RESULTS

A systematic analysis of material responses is carried out. Comparisons with experimental results are made when applicable. Section 3.1 describes results from the mesoscale model for the local material responses at the particle and interparticle level and how they are affected by changes in material attributes such as particle size and particle loading. A parametric study is conducted to determine reaction behavior over a range of particle size and particle loading. The results are used to determine the burn rate at the interparticle scale and Arrhenius model parameters for the coarse-grained model.

Downloaded from pubs.acs.org/jpccck/article-pdf/130/26/8972/6516108/acs.jpcc.6c00580.pdf by UNIV OF CALIFORNIA RIVERSIDE user on 29 August 2026

https://doi.org/10.1021/acs.jpcc.6c00580
J. Phys. Chem. C 2026, 130, 8972−8986

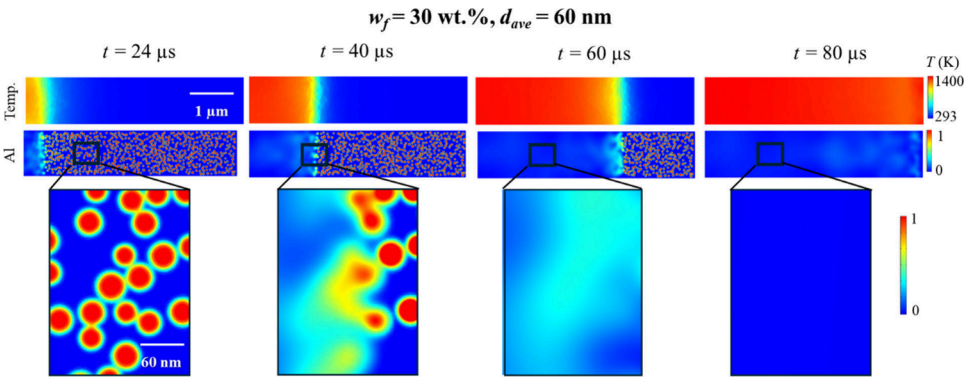

Figure 4. Distributions of temperature and Al species at four different times for a sample with a solids loading of 30 wt % and particle diameter of 60 nm.

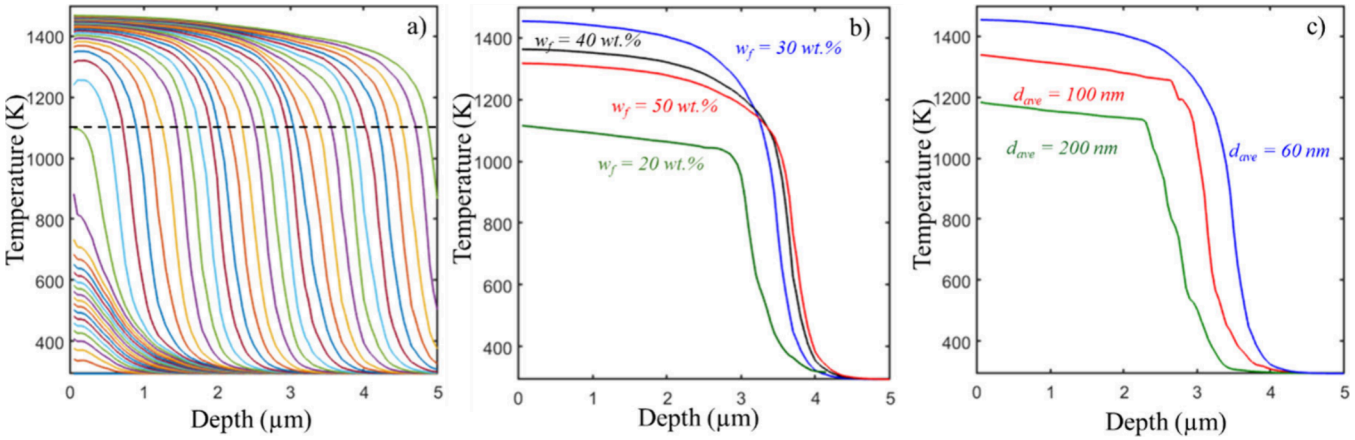

Figure 5. a) Profiles of average temperature at different times for the sample in Figure 4 (30 wt % Al, d_{ave} = 60 nm) used to evaluate burn rate. The dashed line represents the reference temperature used for the burn rate calculation. b) Comparison of temperature distributions at t = 60 μs for samples with different solids loadings (green-20 wt %, blue-30 wt %, black-40 wt %, red-50 wt %), the particle size is d_{ave} = 60 nm. c) Comparison of temperature distributions at t = 60 μs for samples with different particle sizes (d_{ave} = 60 nm (blue), 100 nm (red), and 200 nm (green)) and the same solids loading of 30 wt %.

The mesoscale and coarse-grained responses are compared. Section 3.3 compares the results from the coarse-grained model with experimental results. The quantities of interest compared are temperature distribution, maximum temperature, reaction front (flame front) thickness, and corrugation of the reaction front. The effects of heterogeneities in terms of region-to-region solids loading fluctuations or particle agglomeration on the flame front are delineated. It is shown that particle density fluctuations at the 150−300 μm size scale directly cause reaction front corrugation and masks the solids loading effects on average burn rate, thereby providing an explanation for the perplexing experimental observation that the average burn rate only weakly depends on solids loading − in contrast to previous experimental results.[11] In Section 3.3, the analysis focuses on the relative influence of diffusion and reaction rate to identify the mechanism that limits the reaction process. Part of the analysis involves mapping the heat and mass flow at the mesoscale. The results show that the reaction process is limited by diffusion at both scales.

3.1. Mesoscale Behavior

The first step in understanding the underlying mechanisms of the reaction process is to understand how the material responds to excitation at a resolution that can explicitly capture microstructural effects at the particle and interparticle level. The mesoscale model is designed to have a sufficiently fine spatial and time resolution, such that it directly resolves the particle-binder distribution over a material microstructure region of 1 μm × 5 μm, as seen in Figure 2. This model size covers approximately 5−16 particles (depending on particle size) in the width direction and 25−80 particles in the length direction. Therefore, it is fine enough to capture the initial heating, mass diffusion, hotspot development, and reaction initiation at the individual particles and particle-binder interfaces. On the other hand, the model is also sufficiently large to capture the mass and heat flow and the reaction propagation between particles and over many particles, such that an approximate steady reaction propagation progress is reached and captured.

Figure 4 shows the mesoscale reaction initiation and progression in a sample with 30 wt % Al and an average particle diameter of 60 nm. The left edge is heated to a temperature of 1100 K to emulate the effect of heating by a hot wire until reaction can sustain the temperature at values at or above this value. The images capture the evolution of the temperature field and the distribution of Al mass fraction between 24 and 80 μs. Four stages of response are observed. The first stage (~0−24 μs) entails initial heating and melting, the second stage (~24−40 μs) involves particle displacement and clustering, the third stage (~40−60 μs) is primarily steady reaction propagation, and the fourth stage (~60−80 μs) is

Downloaded from pubs.acs.org/jpccck/article-pdf/130/26/8972/6516108/acs.jpcc.6c00580.pdf by UNIV OF CALIFORNIA RIVERSIDE user on 29 August 2026

https://doi.org/10.1021/acs.jpcc.6c00580
J. Phys. Chem. C 2026, 130, 8972−8986

continued steady-state propagation until complete consumption of the sample. A reaction is considered self-sustaining if it attains a steady-state of propagation and reaches the end of the sample, as shown in the last step in Figure 4. The characteristic length and time scales for reaction initiation and propagation for reaching a steady-state reaction front are ~1.8 μm and ~24 μs in Figure 4. These values are dependent on both particle size and solids loading, as discussed later.

The distributions of temperature along the length of the sample in Figure 4 at 4 different times with an increment of 2 μs are shown in Figure 5a. The values are averages over the sample width. To evaluate burn rate, a reference temperature of 1100 K (dashed line) is used. This approach is reasonable as the temperature profiles at different times in the steady-state propagation stage are similar to each other. The burn rate is taken as the distance traveled by the front divided by the time increment. The values over a range of time are averaged to provide the burn rate for that sample. Particle size and solids loading significantly affect the temperature distribution and burn rate. This effect is examined in Figure 5b and c which compare the distributions of temperature at t = 60 μs for samples with different solids loadings and different particle diameters, respectively. For the same particle size (Figure 5b), the peak temperature is slightly lower and the propagation is slightly faster when the solids loading is higher. The particle size over the range analyzed appears to have a more significant effect (Figure 5c). Specifically, smaller particle sizes lead to higher peak temperatures and faster propagation rate. Particle size also has a clear influence on the burn front thickness and temperature gradient, with smaller particles leading to thinner and steeper fronts. For the cases in Figure 5c, the highest reaction front temperature gradient is −937, −924, and −899 K/μm for particle size of 60, 100, and 200 nm, respectively. Lower slopes reflect the slower reaction response of larger particles. The trend is consistent with what is observed in the experiments.

The time and propagation distance required for the reaction front to reach a steady state are useful measures for comparing the influences of different factors. These quantities are evaluated and compared for different particle sizes and solids loadings. Figure 6a and b show, respectively, the distance of propagation (or depth into the material from the left edge of the sample) and time required to reach steady state as functions of solids loading for the three particle sizes analyzed.

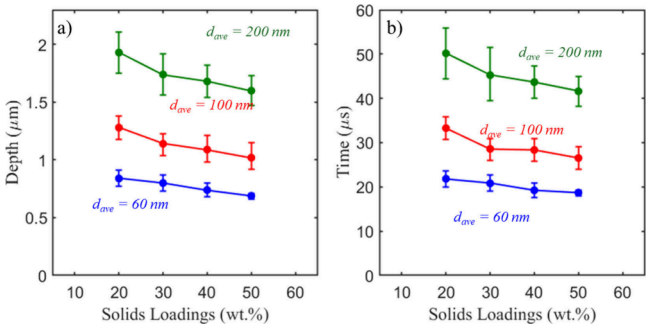

Figure 6. a) Distance of reaction front propagation required for reaction to reach steady state as a function of solids loading for the particle sizes of d_{ave} = 60 nm (blue), 100 nm (red), and 200 nm (green). b) Time of reaction front propagation required for reaction to reach steady state as a function of solids loading for the same three particle sizes.

Materials with larger particles take longer to reach steady-state burning in terms of both propagation distance and time. On average, the critical distance of propagation for reaching steady state for d_{ave} = 200 nm and d_{ave} = 100 nm are 2.23 and 1.38 times that for d_{ave} = 60 nm, respectively. Similarly, on average the critical time for d_{ave} = 200 nm and d_{ave} = 100 nm are 2.12 and 1.31 times that for d_{ave} = 60 nm, respectively. On the other hand, the rate of decrease of the distance with solids loading is 0.006 μm/wt % and the rate of decrease of the time with solids loading is 0.156 μs/wt %. The figures also show that larger particles lead to higher fluctuations in the data.

Figure 7 shows the effects of solids loading and particle size on burn rate. For comparison, the experimental data from Part I is also shown.[10] Over the ranges analyzed, particle size has a much larger influence on burn rate than solids loading. Larger particles reduce burn rate and increase scatter in the calculated burn rate. This is not surprising as particle size is known to affect the reaction kinetics of a system.[54−56] On average, the burn rates for d_{ave} = 200 nm and d_{ave} = 100 nm are 74% and 86% of that for d_{ave} = 60 nm at the same solids loading. Solids loading, on the other hand, has a much smaller effect on burn rate, especially in the fuel-rich cases studied in Part I. Specifically, the average burn rate only increases by ~0.3 cm/s for d_{ave} = 100 nm (4.7 to 5.01 cm/s) and d_{ave} = 60 nm (5.44 to 5.76 cm/s). For d_{ave} = 200 nm, the average burn rate is ~4.2 cm/s over the range of solids loading analyzed, with a higher degree of data scatter. The 20 wt % case, which is not included in Part I, and the other cases together show that burn rate in the fuel-lean regime is more strongly dependent on solids loading. This trend is more pronounced at larger particle sizes, because interparticle distances increase with particle size at the same solids loading.

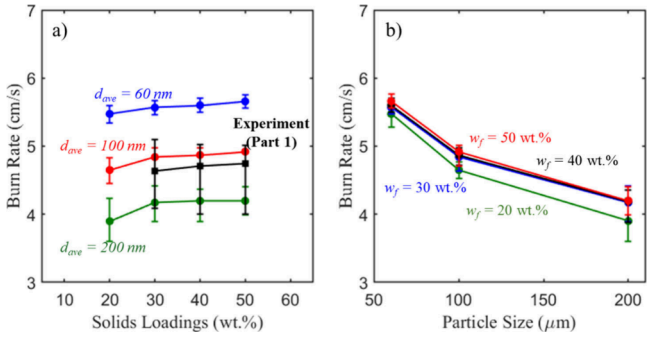

Figure 7. Burn rate as a function of a) solids loading for the particle sizes of d_{ave} = 60 nm (blue), 100 nm (red), and 200 nm (green); and b) particle size for the solids loadings of w_f = 20 wt % (green), 30 wt % (blue), 40 wt % (black), and 50 wt % (red). The burn rate decreases with increasing particle size and is relatively less sensitive to solids loading.

Larger interparticle distances require the reaction front to traverse more low thermal conductivity PVDF to reach the next particle, reducing the overall energy release rate and slowing the burn rate. Overall, the results for d_{ave} = 100 nm are consistent with data from the experiments, except that the experimental data set shows a higher degree of scatter than the mesoscale results in Figure 7. The reason for this will be further explored in Section 3.3 using coarse-grained scale model results with higher-scale particle density fluctuations.

The mesoscale results are also used to obtain parameters for a homogenized Arrhenius chemical kinetics model to be used

Downloaded from pubs.acs.org/jpccck/article-pdf/130/26/8972/6516086/acs.jpcc.6c00580.pdf by UNIV OF CALIFORNIA RIVERSIDE user on 29 August 2026

https://doi.org/10.1021/acs.jpcc.6c00580
J. Phys. Chem. C 2026, 130, 8972−8986

as input at the coarse-grained scale, thereby allowing larger size scales and longer physical times to be reached. The objective is to be able to account for larger-scale region-to-region particle density fluctuations. The extraction of the homogenized reaction model parameters uses the burn rate results discussed above for different particle sizes and solids loading levels. The task is carried out in a manner that ensures that homogenized simulations carried out using the extracted parameters for the particle size and density conditions of the mesoscale calculations closely match the results of the mesoscale calculations.

Figure 8a shows a comparison of the results from a mesoscale calculation and a corresponding coarse-grained

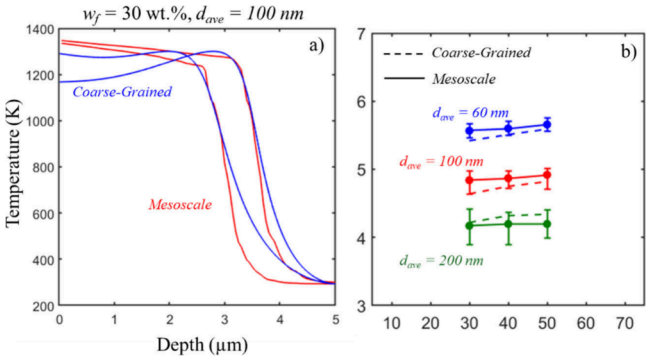

Figure 8. a) Comparison of temperature profiles at t = 50 and 60 μs from a mesoscale calculation and the corresponding coarse-grained calculation for d_{ave} = 100 nm and w_f = 30 wt %; b) comparison of burn rate from the mesoscale and coarse-grained calculations.

model calculation of the same sample dimensions of 1 × 5 μm, same solids loading of 30 wt %, and same particle diameter of 100 nm. It can be seen that the homogenized calculation yields results that capture the primary features of the mesoscale model results in terms of the burn rate and the peak temperature, with the homogenized model showing a slightly lower temperature gradient at the leading edge of the burn front due to the homogenized treatment of thermal conduction. Since the homogenized model is primarily used to study the structure of the burn front over larger scales, the accuracy in capturing the burn rate is the most important consideration. As shown in Figure 8b, this is well achieved. The Arrhenius relation parameters so obtained from the mesoscale result for the coarse-grained model are summarized in Table 5.

Table 5. Arrhenius Relation Parameters for the Coarse-Grained Model

particle size	frequency factor (A) ($m^9/(mol^3 \cdot s)$)	activation energy (E) (kJ/mol)	enthalpy of reaction (ΔH) (kJ/mol)
60	7.5×10^3	171	9
100	3.4×10^3	178	9
200	8.8×10^2	187	9

3.2. Macroscopic Behavior

To account for the larger-scale solids loading variations at the overall sample size scale of millimeters, coarse-grained models illustrated in Figure 2 and described in Section 2.1 are used. The significantly higher range of scatter in the experimental data for burn rate shown in Figure 7a cannot be fully accounted for by the mesoscale calculations. The information gained from the mesoscale is used to inform the higher-scale models. Part of the reason that burn rate is obscured can be due to particle clustering (particle agglomeration) at size scales of 10s to 100s μm. Particle-explicit models at such scales would be computationally prohibitive and impractical. The coarse-grained simulations carried out concern the material setting combinations stated in Table S1. The flame structure, corrugation, and burn rate for these material settings are discussed below.

Figure 9a–c shows direct comparisons of the steady-state temperature profiles from coarse-grained simulations and experiments[10] for the three cases of 30H, 40H, and 50H from Table S1. The simulations capture the basic shape of the temperature distribution in terms of peak temperature (Figure 9d) and burn front thickness (Figure 9e). The peak temperature is the highest (2423 K) around the balanced stoichiometric condition ($w_{f\text{-AVE}}$ = 30 wt %) and decreases monotonically to 2185 K as $w_{f\text{-AVE}}$ increases to 50 wt %. The burn front thickness is calculated by measuring the distance from the intersection between unreacted region and the reaction zone (point B in Figure 9) to the peak temperature location (point A in Figure 9). The thickness increases from 162 to 205 μm as the solids loading increases from 30 wt % to 50 wt %. The increase is 98 to 150 μm in experiments over the same range of solids loading. Although the calculated values are higher than the measured values, both show the same trend. The peak temperatures shown in Figure 9d are generally in agreement with experimental measurements. The differences between the calculated and measured temperature profiles can be attributed to several factors. A simplified chemical reaction treatment likely contributes to the differences by lumping all reaction and endothermic steps into one kinetics model, one latent heat associated with decomposition, and one latent heat associated with melting of Al. Other factors may include mechanisms of heat and mass loss not modeled, such as convective losses at surfaces. Assumptions made in generating the coarse-grained particle density variations and the lack of directly measured density variations in the samples used in the experiments may also contribute to the observed discrepancies. These factors should be considered in the future.

The effect of spatial variation of solids loading (as measured by $\upsilon_{var.}$, see Table S1) on temperature distribution at the burn front is shown in Figure 10. The analysis focuses on how the level of region-to-region fluctuation in solids loading affects the burn front structure. Figure 10a–c shows three coarse-grained microstructure cases (microstructures A and J in Table S1) with the same spatial wavelength ($\lambda_{cluster}$ = 600 μm) and size ($d_{cluster}$ = 150 μm) of particle cluster (see Figure 2 for illustration) and the same average solids loading (w_{f_ave} = 40 wt %). The difference is in the amplitude of the solids loading variation ($\upsilon_{var.}$) which is 0, 5, and 10 wt %, respectively. $d_{cluster}$ is the average diameter of particle clusters with similar solids loading values. The boundaries of these regions correspond to particle densities 5% from the relevant maximum/minimum solids loading values ($w_{f\_ave} \pm \upsilon_{var.}$). The average center-to-center distance among the clusters is $\lambda_{cluster}$.

Figure 10d–f shows the steady-state temperature distributions at $t \approx 115$ ms for the three microstructures in Figure 10a–c, respectively. To quantify the structure of the burn front, a boundary line within the active reaction zone is identified. For consistency in the analyses, this line is taken as the contour with a temperature of 1600 K, considered the

Downloaded from pubs.acs.org/jpccck/article-pdf/130/26/8972/6516108/acs.jpcc.6c00580.pdf by UNIV OF CALIFORNIA RIVERSIDE user on 29 August 2026

https://doi.org/10.1021/acs.jpcc.6c00580
J. Phys. Chem. C 2026, 130, 8972–8986

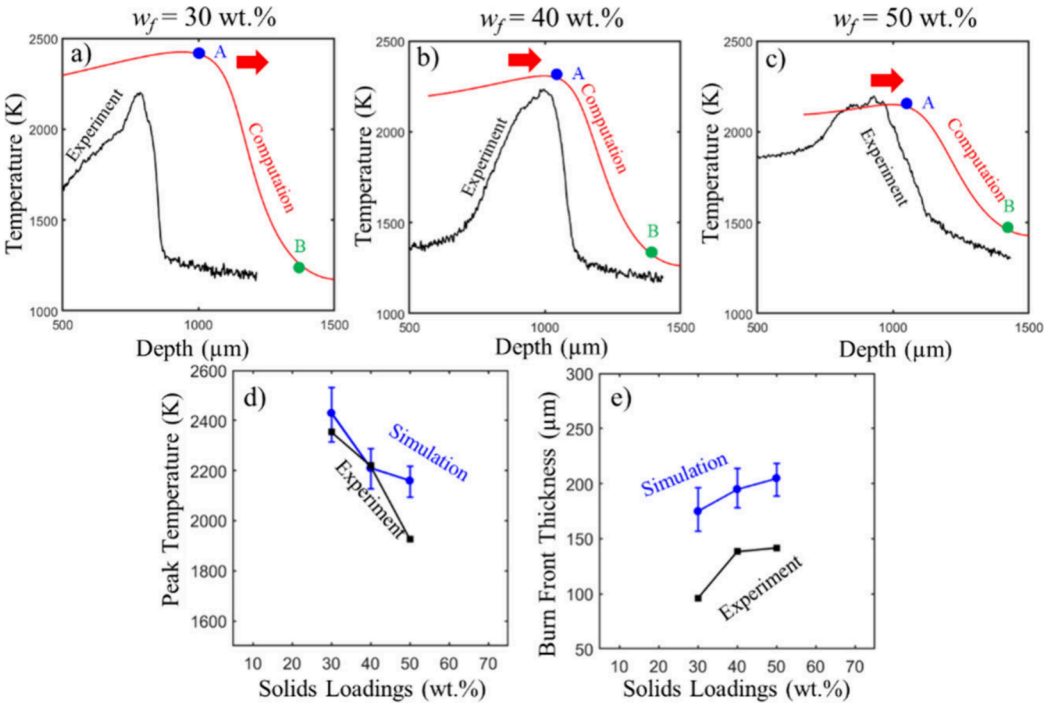

Figure 9. Comparisons of calculated and measured temperature profiles for a) 30, b) 40, and c) 50 wt % solids loadings. The distance between points A and B is taken as the burn front thickness, with A being the location of peak temperature and B being the point separating the reaction zone and unreacted region. Comparisons of calculated and measured d) peak temperature and e) burn front thickness over the same range of solids loading.

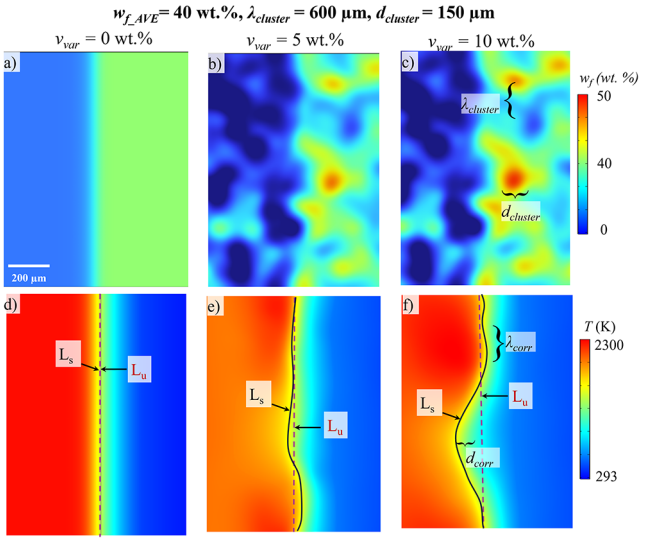

Figure 10. a–c) Coarse-grained microstructures with different amplitudes of Al particle loading fluctuation and the same average solids loading of 40 wt %, cluster wavelength of $\lambda_{cluster}$ = 600 μm, and cluster diameter of $d_{cluster}$ = 150 μm. d–f) Distributions of temperature at t = 115 ms for the three microstructures, respectively. The instantaneous (L_s) and average (L_u) burn fronts are shown along with $\lambda_{cluster}$, $d_{cluster}$, λ_{Burn}, and d_{Burn}.

actual burn front, and is denoted by L_s. The average burn front position is a straight line denoted by L_u. The ratio L_s/L_u is referred to as the corrugation whose values are between ~1.1 and 1.2 in the experiments. The variables λ_{corr} and d_{corr} are the wavelength and amplitude of the burn front L_s. When there is no clustering (particles are uniformly distributed at w_{f_ave}, i.e., $v_{var.}$ = 0 wt %), the reaction front is flat and the corrugation is 1 (Figure 10d). Increasing $v_{var.}$ to 5 wt % (Figure 10e) causes d_{corr} to increase to ~10 μm and the corrugation to increase to ~1.05. Further increasing $v_{var.}$ to 10 wt % causes the d_{corr} to reach ~100 μm and the corrugation to increase to ~1.22 (Figure 10f).

Figure 11a shows the correlation between the burn front wavelength and the cluster wavelength for microstructures with an average solids loading of 40 wt %. Three cluster wavelengths (600, 800, and 1000 μm), two solids loading fluctuation amplitudes (5 and 10 wt %), and two cluster sizes (150 and 500 μm) are considered. The data points fall along the 45° line which represents perfect one-to-one correspondence between the two measures, indicating close correlation between the two and the fact that burn front corrugation is due to particle clustering. The burn front wavelength deviates from the particle cluster wavelength most when the cluster wavelength and the solids loading variation amplitude are low (e.g., 40 ± 5 wt %, 600, 500, and 40 ± 5 wt %, 600, 150). For these two cases, the burn front wavelength is 1.38 and 1.31 times the respective cluster wavelength. In general, larger cluster sizes and higher particle solids loading fluctuations lead to higher amplitudes of burn front corrugation, and the effects of the two tend to superimpose or even reinforce each other, see Figure 11b. For example, clusters with a size of $d_{cluster}$ = 500 μm result in burn front amplitude that is ~ 1.81 times that for $d_{cluster}$ = 150 μm. A cluster solids loading variation of $v_{var.}$ = 5 wt % leads to a burn front amplitude that is 45% that for $v_{var.}$ = 10 wt %. As solids loading increases the burn front amplitude is less affected by solids loading variation. The peak d_{corr} achieved in the same microstructure ($\lambda_{cluster}$ = 600 μm and $d_{cluster}$ = 500 μm) is 121 μm, 88 μm (shown in Figure 11b), and 64 μm, for solids loading of 30, 40, and 50 wt % respectively. Because the structure of the burn front evolves as the reaction propagates,

https://doi.org/10.1021/acs.jpcc.6c00580
J. Phys. Chem. C 2026, 130, 8972–8986

Downloaded from pubs.acs.org/jpccck/article-pdf/130/26/8972/6516086/acs.jpcc.6c00580.pdf by UNIV OF CALIFORNIA RIVERSIDE user on 29 August 2026

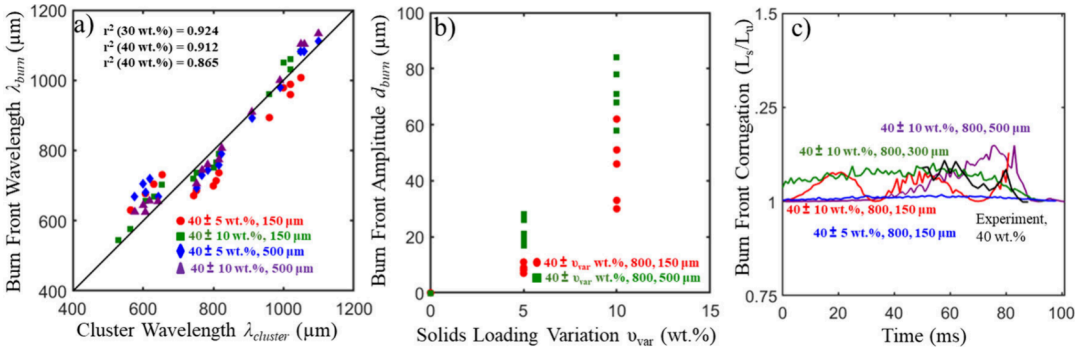

Figure 11. a) Correlation between cluster wavelength and burn front wavelength, b) dependence of amplitude of burn front corrugation on solids loading fluctuation amplitude, and c) histories of burn front corrugation for microstructures (D, M, N, and O in Table S1) with a solids loading of 40 wt % but different amplitudes and wavelengths of particle loading fluctuation.

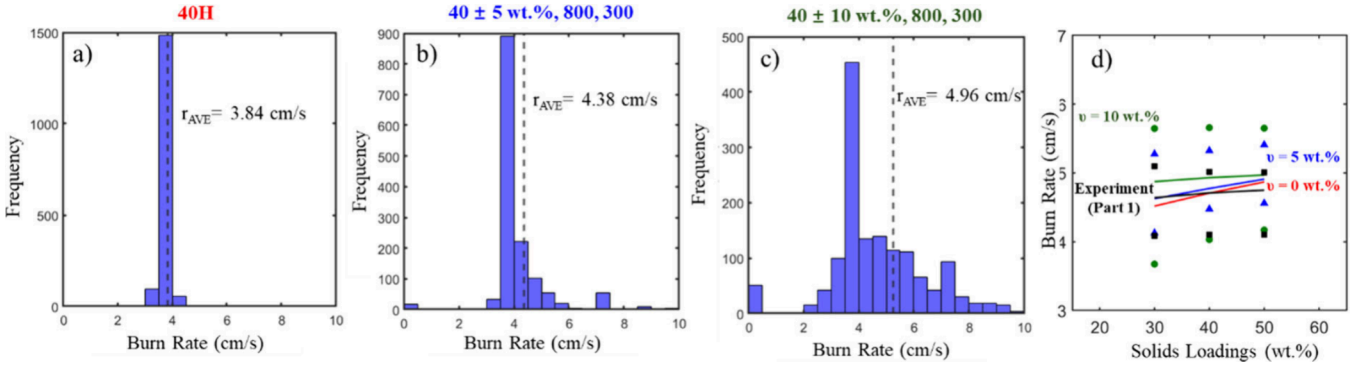

Figure 12. Distributions of local burn rate for microstructures with an average solids loading of w_{f_AVE} = 40 wt %, spatial wavelength of $\lambda_{cluster}$ = 800 μm, and cluster size of $d_{cluster}$ = 300 μm and different solids loading fluctuation levels, a) $\upsilon_{var.}$ = 0 wt % (homogeneous), b) $\upsilon_{var.}$ = 5 wt % (E in Table S1), and c) $\upsilon_{var.}$ = 10 wt % (N in Table S1). d) average (solid line) and range (markers) of local burn rate as functions of solids loading for microstructures with solids loading fluctuation levels of $\upsilon_{var.}$ = 0 wt % (red), $\upsilon_{var.}$ = 5 wt % (blue), and $\upsilon_{var.}$ = 10 wt % (green). Experimental results (black) are also shown.

slight variations in the burn front corrugation occur over time. The histories of the corrugation for several microstructure cases with attributes tracking those of the material used in experiments are shown in Figure 11c, along with the experimental measurements. The results are in general qualitative agreement with each other.

3.2.1. Burn Rate. Experiments[10] have outlined the differences between the average (global) burn rate $r_b^{(global)}$ and the microscale (local) burn rate $r_b^{(micro)}$. The latter is calculated from the displacements of individual points along the burn front and the former is the velocity of the average front L_u (Figure 10). The coarse-grained model lends itself to systematic analyses of both burn rate measures in a consistent and unifying manner. The burn rates discussed in Figure 12 are calculated over the shortest distance between individual points on successive burn fronts, following the same methodology used in experiments outlined in Figure 5 of ref 10.

Figure 12a–c shows the distributions of the local burn rate, $r_b^{(micro)}$, for three coarse-grained microstructures with the same average solids loading (w_{f_AVE} = 40 wt %), spatial wavelength ($\lambda_{cluster}$ = 800 μm), and cluster size ($d_{cluster}$ = 300 μm) but different levels of particle cluster fluctuation $\upsilon_{var.}$. These microstructure cases show burn front corrugations similar to those observed in the experiments (Figure 11c). In the baseline (homogeneous) case ($\upsilon_{var.}$ = 0), the burn rate is essentially uniform with an average of 3.84 cm/s. At a solids loading fluctuation of $\upsilon_{var.}$ = 5 wt % (E in Table S1), the local burn rate varies between 3.71 and 9.5 cm/s with an average of 4.38 cm/s. At $\upsilon_{var.}$ = 10 wt % (N in Table S1), the burn rate varies between 2.1 cm/s and ~ 10 cm/s with an average of 4.96 cm/s. Higher levels of particle density fluctuation cause wider spreads of the local burn rate. The most dominant value is ~3.9 cm/s for all three cases, consistent with experiments. On the other hand, when the level of solids loading fluctuation is kept the same (at $\upsilon_{var.}$ = 5 or 10 wt %) and the average solids loading is varied (w_{f_AVE} = 30, 40, or 50 wt %), the average burn rate increases slightly and the spread of the local burn rate remains similar, consistent with experimental data. This trend is seen in Figure 12d which shows the calculated burn rate as a function of solids loading for the three solids loading fluctuation levels (0, 5, and 10 wt %). The dependence of the average burn rate on solids loading decreases as the level of particle density fluctuation $\upsilon_{var.}$ increases. Specifically, the slope of the average burn rate line in Figure 12d is 0.4 cm/(s·wt %) for $\upsilon_{var.}$ = 0 wt %, 0.35 cm/(s·wt %) for $\upsilon_{var.}$ = 5 wt %, and 0.18 cm/(s·wt %) for 10 wt %. The reason for this change in slope is that the wider spread of the local burn rate and the associated uncertainties "masked" the dependence of the overall burn rate on solids loading. Specifically, more corrugated burn fronts involve higher proportions of local burn propagation in directions at higher angles away from the macroscopic direction of propagation, leading to lower velocities of the average burn front (L_u).

https://doi.org/10.1021/acs.jpcc.6c00580
J. Phys. Chem. C 2026, 130, 8972−8986

Downloaded from pubs.acs.org/jpccck/article-pdf/130/26/8972/6516108/acs.jpcc.6c00580.pdf by UNIV OF CALIFORNIA RIVERSIDE user on 29 August 2026

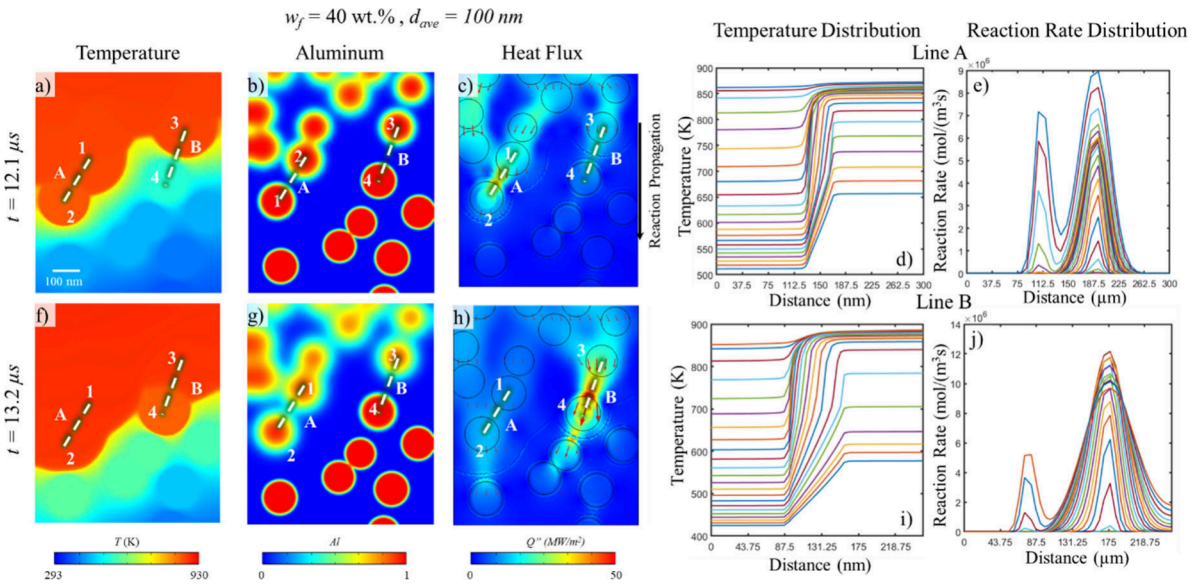

Figure 13. Distributions of temperature, aluminum species concentration, and heat flux at t = 12.1 and 13.2 μs in a region of a mesoscale microstructure with a solids loading of 40 wt % and an average particle size of d_{ave} = 100 nm. The temperature front follows the particles closely with the heat flux generally flowing to the closest particle in the direction of reaction propagation (top to bottom). The temperature and reaction rate profiles between the two particle pairs are also shown.

3.3. Rate Limiting Mechanism

The reaction propagation rate depends on the interplay of several processes, the most important of which are diffusion, which leads to mixing of the reactants, and chemical kinetics, which relate to the rate of heat release. It is important to determine which of these processes is the limiting process (or "bottleneck") at the mesoscale. To this end, the mesoscale model is used to analyze the events in the reaction zone as it moves through the material. To illustrate the mesoscale processes, Figure 13 shows the distributions of temperature, Al concentration, and heat flux at t = 12.1 and 13.2 μs in a region of a sample with a solids loading of 40 wt % and particle diameters of d_{ave} = 100 nm. The direction of reaction propagation is from top to bottom. The particles of interest are labeled 1−4. The distance between the two pairs of particles (1−2 and 3−4) is ∼152 nm which is slightly greater than the average NND calculated in Section 2.1. At t = 12.1 μs (Figure 13a−c), particles 1 and 3 have just entered the reaction front. Particle 2 is on the edge of the reaction front, and particle 4 is still in the unreacted region. Figure 13c and h show the magnitude and direction of the heat flux at the two times. The black outlines are the initial positions of aluminum particles. The direction of significant heat flow is always toward the nearest unreacted particle in the direction of reaction propagation. The magnitude of the heat flux is on the order of 23 MW/m^2 but can approach 50 MW/m^2. In large particle-free gaps, such as the one in Figure 13, less heat generation and conduction occur, causing the reaction front to go around the gap. The gap is eventually filled by lateral heat conduction. Obviously, Al-poor regions delay the propagation of the reaction front.

The local temperature and reaction rate profiles along the lines connecting the centers of the two particle pairs (line A for particles 1−2, line B for particles 3−4) are calculated and shown in Figure 13d−e and i−j. The profiles at 20 different times are shown at 0.05 μs increments. The temperature within each particle is relatively uniform due to the high thermal conductivity of Al. Between two particles, a temperature gradient forms (Figure 13d and i). The temperature front moves through the material at an average velocity of ∼3.9 cm/s. As elevated temperatures reach the next particle, chemical reaction initiates. Particles 2 and 4 are initially detached from the reaction front and reach an internal temperature between 550 and 600 K before the reaction front reaches them. Aluminum particles ahead of the reaction front may act as heat sinks, directing the heat flow. There is also a slight delay between when the temperature front reaches a particle surface and when reaction initiates. This delay is ∼0.53 μs for 200 nm particles, ∼0.4 μs for 100 nm particles, and ∼0.18 μs for 60 nm particles. This delay and the fact that reactions are limited to the particle surfaces are because diffusion between the particle and the PVDF is necessary and takes time. Thus, reaction initiation in large particle-free gaps is slower, raising the likelihood that the reaction is species diffusion-limited. A further analysis of the Damköhler number for this system (both mesoscale and coarse-grained) and a sensitivity analysis are included in the Supporting Information.

4. CONCLUSIONS

A multiscale framework is developed to study the reaction initiation and burning in the Al/PVDF reactive composite system. The framework integrates mutually reinforcing models at two size scales to resolve reaction development and propagation. The two models have distinct spatial resolutions: the mesoscale model provides explicit resolution of the particle−polymer heterogeneous microstructure (including size distribution and volume fraction) and focuses on the material response at the particle and interparticle levels (∼5 μm), and the coarse-grained model phenomenologically captures the effects of particle agglomeration and density fluctuations at higher length scales (∼1500 μm). This framework explicitly captures the effects of particle size and solids loading (mesoscale), solids loading fluctuation (coarse-grained scale), and reaction kinetics on both the process leading to the attainment of steady-state reaction and the process of steady-state burn front propagation. Uncertainty in

https://doi.org/10.1021/acs.jpcc.6c00580
J. Phys. Chem. C 2026, 130, 8972−8986

Downloaded from pubs.acs.org/jpcccck/article-pdf/130/26/8972/6516086/acs.jpcc.6c00580.pdf by UNIV OF CALIFORNIA RIVERSIDE user on 29 August 2026

the material behavior is quantified by using multiple statistically equivalent microstructure samples at each material setting. The objective is to understand the importance of the different mechanisms that affect ignition and burn front propagation through the material.

The mesoscale simulations focus on microstructures with particle diameters in the range of 60−200 nm and solids loadings from 20 to 50 wt %. The results led to the quantification of the time and distance necessary for the formation of a steady-state temperature front and the burn rate during the subsequent steady state propagation process. A clear particle size effect is observed. Specifically, the local burn rate decreases from ∼5.5 to 4 cm/s as particle size increases from 60 to 200 nm. Particle size increases in this range also cause the sensitivity of burn rate to solids loading to decrease, with the slope of the burn rate vs solids loading relation decreasing from 0.2 to 0.06 cm/s/wt % over the range of solids loading of 30 wt % to 50 wt %.

Results from the mesoscale model are also used to inform the higher-scale coarse-grained model through calibrated parameters for reaction kinetics. The heterogeneities considered in the coarse-grained model are in the form of region-to-region particle density fluctuations due to agglomeration or clustering. The specific conditions analyzed involve average solids loadings between 30 and 50 wt %, region-to-region solids loading fluctuations between 0 and 10 wt % relative to the averages, particle cluster sizes between 150 and 500 μm, and wavelengths of particle clustering between 600 and 1000 μm. The resulting temperature rise, temperature distributions, and reaction zone thickness agree with experimental measurements. The results also show that solids loading, solids loading fluctuations, and particle clustering affect the flame front corrugation, such that higher solids loading fluctuations, shorter spatial wavelengths of particle clustering, and larger particle cluster sizes lead to higher flame front corrugation and lower average burn rates. The consequence of these effects is significant scatter in the burn rate, which leads to the average burn rate showing a weaker dependence on solids loading than what is seen at the mesoscale or when the particles are uniformly distributed (without clustering). This finding provides an explanation for the same trend observed in the companion experiments.

Overall, the multiscale framework developed here is applicable to other reactive metal−polymer systems. The results of a systematic parametric study of the interplays between the microstructure and material attributes will be reported in the future.

■ ASSOCIATED CONTENT

Supporting Information

The Supporting Information is available free of charge at https://pubs.acs.org/doi/10.1021/acs.jpcc.6c00580.

Table of coarse-grained model names; graphs containing temperature-dependent material properties; particle NND histograms; Damköhler number investigation; coarse-grained sensitivity study (PDF)

■ AUTHOR INFORMATION

Corresponding Author

Min Zhou − *The Woodruff School of Mechanical Engineering and School of Materials Science and Engineering, Georgia Institute of Technology, Atlanta, Georgia 30332, United States*; Email: min.zhou@gatech.edu

Authors

Daniel Olsen − *The Woodruff School of Mechanical Engineering and School of Materials Science and Engineering, Georgia Institute of Technology, Atlanta, Georgia 30332, United States*

Erik Hagen − *Materials Science and Engineering, University of California, Riverside, California 92521, United States*

Michael R. Zachariah − *Materials Science and Engineering, University of California, Riverside, California 92521, United States; Department of Chemical and Environmental Engineering, University of California, Riverside, California 92521, United States;* orcid.org/0000-0002-4115-3324

Complete contact information is available at: https://pubs.acs.org/10.1021/acs.jpcc.6c00580

Notes

The authors declare no competing financial interest.

■ ACKNOWLEDGMENTS

This research was sponsored by and was accomplished under the Air Force Office of Scientific Research (AFOSR) under the Multi-University Research Initiative (MURI) Grant No. FA9550-19-1-0008 as well as a single investigator grant to M.R.Z. Partial support from Los Alamos National Laboratory Subcontract No. 633534 is also acknowledged.

■ REFERENCES

(1) Berner, M.; Zarko, V. E.; Talawar, M. B. Nanoparticles of energetic materials: synthesis and properties. *Combustion, Explosion, and Shock Waves* **2013**, *49*, 625−647.

(2) Kuo, K. K.; Risha, G. A.; Evans, B. J.; Boyer, E. Potential usage of energetic nano-sized powders for combustion and rocket propulsion. *MRS Online Proceedings Library* **2003**, *800*, 39−50.

(3) Thiruvengadathan, R. Aluminum-based nano-energetic materials: state of the art and future perspectives. *Nano-energetic materials* **2019**, 9−35.

(4) Gnanaprakash, K.; Chakravarthy, S. R.; Sarathi, R. Combustion mechanism of composite solid propellant sandwiches containing nano-aluminium. *Combustion and flame* **2017**, *182*, 64−75.

(5) Saniger, J. M.; Sánchez, N. A.; Flores, J. O. Partial fluorination of γ-alumina by gaseous fluorine. *J. Fluorine Chem.* **1998**, *88* (2), 117−125.

(6) Padhye, R.; Aquino, A. J.; Tunega, D.; Pantoya, M. L. Fluorination of an alumina surface: modeling aluminum−fluorine reaction mechanisms. *ACS Appl. Mater. Interfaces* **2017**, *9* (28), 24290−24297.

(7) Huang, S.; Hong, S.; Su, Y.; Jiang, Y.; Fukushima, S.; Gill, T. M.; Yilmaz, N. E. D.; Tiwari, S.; Nomura, K.-i.; Kalia, R. K.; Nakano, A.; Shimojo, F.; Vashishta, P.; Chen, M.; Zheng, X. Enhancing combustion performance of nano-Al/PVDF composites with β-PVDF. *Combust. Flame* **2020**, *219*, 467−477.

(8) Shi, K.; Wang, Y.; Zachariah, M. R. Microwave antenna focusing for spatially resolved modulation of burn rate. *Chemical Engineering Journal* **2024**, *492*, No. 152192.

(9) Collard, D. N.; Fleck, T. J.; Rhoads, J. F.; Son, S. F. Tailoring the reactivity of printable Al/PVDF filament. *Combust. Flame* **2021**, *223*, 110−117.

(10) Hagen, E.; Olsen, D.; Zhou, Y.; Zhou, M.; Zachariah, M. Combustion Reaction Dynamics of Nano-Aluminum and PVDF Composites, Part I: Experimental Studies at the Microscopic Level. *J. Phys. Chem. C* **2026**, DOI: 10.1021/acs.jpcc.6c00579.

Downloaded from pubs.acs.org/jpccck/article-pdf/130/26/8972/6516086/acs.jpcc.6c00580.pdf by UNIV OF CALIFORNIA RIVERSIDE user on 29 August 2026

(11) Wang, H.; Rehwoldt, M.; Kline, D. J.; Wu, T.; Wang, P.; Zachariah, M. R. Comparison study of the ignition and combustion characteristics of directly-written Al/PVDF, Al/Viton and Al/THV composites. *Combust. Flame* **2019**, *201*, 181−186.
(12) Popenko, E.; Gromov, A.; Shamina, Y. Y.; Il'in, A.; Sergienko, A.; Popok, N. Effect of the addition of ultrafine aluminum powders on the rheological properties and burning rate of energetic condensed systems. *Combustion, Explosion, and Shock Waves* **2007**, *43*, 46−50.
(13) Cohen, N. S. A pocket model for aluminum agglomeration in composite propellants. *AIAA J.* **1983**, *21* (5), 720−725.
(14) Pivkina, A. N.; Frolov, Y. V.; Ivanov, D. A. Nanosized components of energetic systems: structure, thermal behavior, and combustion. *Combustion, Explosion, and Shock Waves* **2007**, *43*, 51−55.
(15) Levitas, V. I. Burn time of aluminum nanoparticles: Strong effect of the heating rate and melt-dispersion mechanism. *Combust. Flame* **2009**, *156* (2), 543−546.
(16) Fukuchi, A. B. Effect of aluminum particle size on agglomeration size and burning rate of composite propellant. *Journal of Thermal Science and Technology* **2022**, *17* (1), 21-00346.
(17) Gao, Y.; Zhu, W.; Wang, T.; Yilmaz, D. E.; Van Duin, A. C. C/H/O/F/Al ReaxFF force field development and application to study the condensed-phase poly (vinylidene fluoride) and reaction mechanisms with aluminum. *J. Phys. Chem. C* **2022**, *126* (27), 11058−11074.
(18) Gallier, S.; Sibe, F.; Orlandi, O. Combustion response of an aluminum droplet burning in air. *Proceedings of the Combustion Institute* **2011**, *33* (2), 1949−1956.
(19) Washburn, E.; Trivedi, J.; Catoire, L.; Beckstead, M. The simulation of the combustion of micrometer-sized aluminum particles with steam. *Combust. Sci. Technol.* **2008**, *180* (8), 1502−1517.
(20) Wang, X.; Hossain, K.; Jackson, T. The three-dimensional numerical simulation of aluminized composite solid propellant combustion. *Combustion Theory and Modelling* **2008**, *12* (1), 45−71.
(21) Bojko, B. T.; Gross, M. L.; Jackson, T. L. Investigating dimensional effects on predicting burning rates of heterogeneous solid propellants. *AIAA J.* **2020**, *58* (4), 1724−1732.
(22) McMurtry, P. A.; Jou, W.-H.; Riley, J.; Metcalfe, R. Direct numerical simulations of a reacting mixing layer with chemical heat release. *AIAA J.* **1986**, *24* (6), 962−970.
(23) Najm, H. N.; Paul, P. H.; Mueller, C. J.; Wyckoff, P. S. On the adequacy of certain experimental observables as measurements of flame burning rate. *Combustion and flame* **1998**, *113* (3), 312−332.
(24) Chakraborty, N.; Hartung, G.; Katragadda, M.; Kaminski, C. Comparison of 2D and 3D density-weighted displacement speed statistics and implications for laser based measurements of flame displacement speed using direct numerical simulation data. *Combust. Flame* **2011**, *158* (7), 1372−1390.
(25) Messer, D. K.; Shin, J. H.; Örnek, M.; Hafner, T. A.; Zhou, M.; Son, S. F. Effects of flexoelectric and piezoelectric properties on the impact-driven ignition sensitivity of P (VDF-TrFE)/nAl films. *Combust. Flame* **2022**, *242*, No. 112181.
(26) Kuklin, V.; Karandashov, S.; Bobina, E.; Drobyshev, S.; Smirnova, A.; Morozov, O.; Danilaev, M. Analysis of aluminum oxides submicron particle agglomeration in polymethyl methacrylate composites. *International Journal of Molecular Sciences* **2023**, *24* (3), 2515.
(27) Kim, S.-C. Analysis of Shielding Performance of Radiation-Shielding Materials According to Particle Size and Clustering Effects. *Applied Sciences* **2021**, *11* (9), 4010.
(28) Dreizin, E. L.; Schoenitz, M. Correlating ignition mechanisms of aluminum-based reactive materials with thermoanalytical measurements. *Prog. Energy Combust. Sci.* **2015**, *50*, 81−105.
(29) Beckstead, M. W.; Liang, Y.; Pudduppakkam, K. Numerical simulation of single aluminum particle combustion. *Combustion, Explosion and Shock Waves* **2005**, *41*, 622−638.
(30) Mullen, J. C.; Brewster, M. Reduced agglomeration of aluminum in wide-distribution composite propellants. *Journal of Propulsion and Power* **2011**, *27* (3), 650−661.
(31) Scokart, P. O.; Selim, S. A.; Damon, J. P.; Rouxhet, P. G. The chemistry and surface chemistry of fluorinated alumina. *J. Colloid Interface Sci.* **1979**, *70* (2), 209−222.
(32) DeLisio, J. B.; Hu, X.; Wu, T.; Egan, G. C.; Young, G.; Zachariah, M. R. Probing the reaction mechanism of aluminum/poly (vinylidene fluoride) composites. *J. Phys. Chem. B* **2016**, *120* (24), 5534−5542.
(33) Yu, H.; Kennedy, E. M.; Mackie, J. C.; Dlugogorski, B. Z. An experimental and kinetic modeling study of the reaction of CHF3 with methane. *Environ. Sci. Technol.* **2006**, *40* (18), 5778−5785.
(34) Li, Z.; Zhao, X.; Li, G.; Gong, F.; Liu, Y.; Yan, Q.; Yang, Z.; Nie, F. Surface fluorination of n-Al particles with improved combustion performance and adjustable reaction kinetics. *Chemical Engineering Journal* **2021**, *425*, No. 131619.
(35) Kharitonov, A. Direct fluorination of polymers—From fundamental research to industrial applications. *Prog. Org. Coat.* **2008**, *61* (2−4), 192−204.
(36) Okino, M. S.; Mavrovouniotis, M. L. Simplification of mathematical models of chemical reaction systems. *Chem. Rev.* **1998**, *98* (2), 391−408.
(37) Feng, Y.; Qin, J.; Liu, S.; Zhang, S.; Li, X.; Cao, Y.; Huang, H. A simplification of pyrolytic reaction model of hydrocarbon fuel and its application in simulation of heated channel flow. *International Journal of Thermal Sciences* **2018**, *130*, 10−18.
(38) Li, D. D.; Wang, C.; Chan, Q. N.; Yeoh, G. H. Soot: A review of computational models at different length scales. *Experimental and Computational Multiphase Flow* **2023**, *5* (1), 1−14.
(39) Knott, M. C.; Craig, A. W.; Shankar, R.; Morgan, S. E.; Iacono, S. T.; Mates, J. E.; McCollum, J. M. Balancing processing ease with combustion performance in aluminum/PVDF energetic filaments. *J. Mater. Res.* **2021**, *36*, 203−210.
(40) Darvey, I. G.; Ninham, B.; Staff, P. Stochastic models for second-order chemical reaction kinetics. The equilibrium state. *J. Chem. Phys.* **1966**, *45* (6), 2145−2155.
(41) Espenson, J. H. *Chemical Kinetics and Reaction Mechanisms*; Citeseer, 1995.
(42) Pellerite, M. J.; Dunbar, T. D.; Boardman, L. D.; Wood, E. J. Effects of fluorination on self-assembled monolayer formation from alkanephosphonic acids on aluminum: kinetics and structure. *J. Phys. Chem. B* **2003**, *107* (42), 11726−11736.
(43) Kim, D. W.; Kim, K. T.; Lee, D.-U.; Jung, S.-H.; Yang, D. Y.; Yu, J. Influence of poly (vinylidene fluoride) coating layer on exothermic reactivity and stability of fine aluminum particles. *Appl. Surf. Sci.* **2021**, *551*, No. 149431.
(44) Chen, S.; Tang, D.-Y.; Zhang, X.-X.; Lyu, J.-Y.; He, W.; Liu, P.; Yan, Q.-L. Enhancing the combustion performance of metastable Al@AP/PVDF nanocomposites by doping with graphene oxide. *Engineering* **2020**, *6* (9), 1019−1027.
(45) *Heat Transfer Module User's Guide: Apparent Heat Capacity Method*; COMSOL Multiphysics, 2020.
(46) Fillo, A. J.; Schlup, J.; Beardsell, G.; Blanquart, G.; Niemeyer, K. E. A fast, low-memory, and stable algorithm for implementing multicomponent transport in direct numerical simulations. *J. Comput. Phys.* **2020**, *406*, No. 109185.
(47) Orekhov, M. Improving molecular dynamics calculation of diffusivity in liquids with theoretical models. *J. Mol. Liq.* **2021**, *322*, No. 114554.
(48) Ewing, M. E.; Isaac, D. A. Thermodynamic Property Calculations for Equilibrium Mixtures. *Journal of Thermophysics and Heat Transfer* **2018**, *32* (1), 118−128.
(49) Crane, C.; Pantoya, M.; Weeks, B.; Saed, M. The effects of particle size on microwave heating of metal and metal oxide powders. *Powder technology* **2014**, *256*, 113−117.
(50) Zhou, W.; Zuo, J.; Ren, W. Thermal conductivity and dielectric properties of Al/PVDF composites. *Composites Part A: Applied Science and Manufacturing* **2012**, *43* (4), 658−664.
(51) Meng, X.-M.; Zhang, X.-J.; Lu, C.; Pan, Y.-F.; Wang, G.-S. Enhanced absorbing properties of three-phase composites based on a thermoplastic-ceramic matrix (BaTiO 3+ PVDF) and carbon black

Downloaded from pubs.acs.org/jpccck/article-pdf/130/26/8972/6516086/acs.jpcc.6c00580.pdf by UNIV OF CALIFORNIA RIVERSIDE user on 29 August 2026

nanoparticles. *Journal of Materials Chemistry A* **2014**, *2* (44), 18725−18730.
(52) Leitner, M.; Leitner, T.; Schmon, A.; Aziz, K.; Pottlacher, G. Thermophysical properties of liquid aluminum. *Metallurgical and Materials Transactions A* **2017**, *48*, 3036−3045.
(53) Erdtman, E.; Satyanarayana, K. C.; Bolton, K. Simulation of α- and β-PVDF melting mechanisms. *Polymer* **2012**, *53* (14), 2919−2926.
(54) Iggland, M.; Leion, H.; Mattisson, T.; Lyngfelt, A. Effect of fuel particle size on reaction rate in chemical looping combustion. *Chemical engineering science* **2010**, *65* (22), 5841−5851.
(55) McIlvried, H.; Massoth, F. Effect of particle size distribution on gas-solid reaction kinetics for spherical particles. *Industrial & Engineering Chemistry Fundamentals* **1973**, *12* (2), 225−229.
(56) Seebauer, V.; Petek, J.; Staudinger, G. Effects of particle size, heating rate and pressure on measurement of pyrolysis kinetics by thermogravimetric analysis. *Fuel* **1997**, *76* (13), 1277−1282.

Downloaded from pubs.acs.org/jpccck/article-pdf/130/26/8972/6516108/acs.jpcc.6c00580.pdf by UNIV OF CALIFORNIA RIVERSIDE user on 29 August 2026

https://doi.org/10.1021/acs.jpcc.6c00580
J. Phys. Chem. C 2026, 130, 8972−8986